Characterization of high-resolution diffractive X-ray optics by ptychographic coherent diffractive imaging

Joan Vila-Comamala,[1,4,*] **Ana Diaz,**[1] **Manuel Guizar-Sicairos,**[1] **Alexandre Mantion,**[2] **Cameron M. Kewish,**[3] **Andreas Menzel,**[1] **Oliver Bunk,**[1] **and Christian David**[1]

[1]*Paul Scherrer Institut, 5232 Villigen PSI, Switzerland*
[2]*BAM Bundesanstalt für Materialforschung und -prüfung, 12200 Berlin, Germany*
[3]*Synchrotron SOLEIL, Saint Aubin BP-48, 91192 Gif-sur-Yvette, France*
[4]*Current Address: X-ray Science Division, Advanced Photon Source, Argonne National Laboratory, Argonne, IL 60439, USA*

[*]*jvila@aps.anl.gov*

Abstract: We have employed ptychographic coherent diffractive imaging to completely characterize the focal spot wavefield and wavefront aberrations of a high-resolution diffractive X-ray lens. The ptychographic data from a strongly scattering object was acquired using the radiation cone emanating from a coherently illuminated Fresnel zone plate at a photon energy of 6.2 keV. Reconstructed images of the object were retrieved with a spatial resolution of 8 nm by combining the difference-map phase retrieval algorithm with a non-linear optimization refinement. By numerically propagating the reconstructed illumination function, we have obtained the X-ray wavefield profile of the 23 nm round focus of the Fresnel zone plate (outermost zone width, $\Delta r = 20$ nm) as well as the X-ray wavefront at the exit pupil of the lens. The measurements of the wavefront aberrations were repeatable to within a root mean square error of 0.006 waves, and we demonstrate that they can be related to manufacturing aspects of the diffractive optical element and to errors on the incident X-ray wavefront introduced by the upstream beamline optics.

OCIS codes: (340.0340) X-ray optics; (050.1965) Diffractive lenses; (100.5070) Phase retrieval; (120.5050) Phase measurement; (340.7460) X-ray microscopy; (340.6720) Synchrotron radiation.

References and links

1. H. C. Kang, H. Yan, R. P. Winarski, M. V. Holt, J. Maser, C. Liu, R. Conley, S. Vogt, A. T. Macrander, and G. B. Stephenson, "Focusing of hard X-rays to 16 nanometers with a multilayer Laue lens," Appl. Phys. Lett. **92**, 221114 (2008).
2. H. Mimura, S. Handa, T. Kimura, H. Yumoto, D. Yamakawa, H. Yokoyama, S. Matsuyama, K. Inagaki, K. Yamamura, Y. Sano, K. Tamasaku, Y. Nishino, M. Yabashi, T. Ishikawa, and K. Yamauchi, "Breaking the 10 nm barrier in hard-X-ray focusing," Nat. Phys. **6**, 122–125 (2010).
3. J. Vila-Comamala, S. Gorelick, E. Färm, C. M. Kewish, A. Diaz, R. Barrett, V. A. Guzenko, M. Ritala, and C. David, "Ultra-high resolution zone-doubled diffractive X-ray optics for the multi-kev regime." Opt. Express **19**, 175–184 (2011).

#152217 - $15.00 USD Received 9 Aug 2011; revised 9 Sep 2011; accepted 12 Sep 2011; published 12 Oct 2011

4. P. Thibault and V. Elser, "X-ray diffraction microscopy," Annu. Rev. Condens. Matter Phys. **1**, 237–255 (2010).
5. K. A. Nugent, "Coherent methods in the X-ray sciences," Adv. Phys. **59**, 1–99 (2010).
6. H. N. Chapman and K. A. Nugent, "Coherent lensless X-ray imaging," Nat. Photonics **4**, 833–839 (2010).
7. J. R. Fienup, "Phase retrieval algorithms: a comparison," Appl. Opt. **21**, 2758–2769 (1982).
8. J. Miao, P. Charalambous, J. Kirz, and D. Sayre, "Extending the methodology of X-ray crystallography to allow imaging of micrometre-sized non-crystalline specimens," Nature **400**, 342–344 (1999).
9. H. M. Quiney, A. G. Peele, Z. Cai, D. Paterson, and K. A. Nugent, "Diffractive imaging of highly focused X-ray fields," Nat. Phys. **2**, 101–104 (2006).
10. G. J. Williams, H. M. Quiney, B. B. Dhal, C. Q. Tran, K. A. Nugent, A. G. Peele, D. Paterson, and M. D. de Jonge, "Fresnel coherent diffractive imaging," Phys. Rev. Lett. **97**, 025506 (2006).
11. J. M. Rodenburg, A. C. Hurst, A. G. Cullis, B. R. Dobson, F. Pfeiffer, O. Bunk, C. David, K. Jefimovs, and I. Johnson, "Hard X-ray lensless imaging of extended objects," Phys. Rev. Lett. **98**, 034801 (2007).
12. P. Thibault, M. Dierolf, A. Menzel, O. Bunk, C. David, and F. Pfeiffer, "High-resolution scanning X-ray diffraction microscopy," Science **321**, 379–382 (2008).
13. P. Thibault, M. Dierolf, O. Bunk, A. Menzel, and F. Pfeiffer, "Probe retrieval in ptychographic coherent diffractive imaging," Ultramicroscopy **109**, 338–343 (2009).
14. C. M. Kewish, M. Guizar-Sicairos, C. Liu, J. Qian, B. Shi, C. Benson, A. M. Khounsary, J. Vila-Comamala, O. Bunk, J. R. Fienup, A. T. Macrander, and L. Assoufid, "Reconstruction of an astigmatic hard X-ray beam and alignment of K-B mirrors from ptychographic coherent diffraction data," Opt. Express **18**, 23420–23427 (2010).
15. C. M. Kewish, P. Thibault, M. Dierolf, O. Bunk, A. Menzel, J. Vila-Comamala, K. Jefimovs, and F. Pfeiffer, "Ptychographic characterization of the wavefield in the focus of reflective hard X-ray optics," Ultramicroscopy **110**, 325–329 (2010).
16. A. Schropp, P. Boye, J. M. Feldkamp, R. Hoppe, J. Patommel, D. Samberg, S. Stephan, K. Giewekemeyer, R. N. Wilke, T. Salditt, J. Gulden, A. P. Mancuso, I. A. Vartanyants, E. Weckert, S. Schöder, M. Burghammer, and C. G. Schroer, "Hard X-ray nanobeam characterization by coherent diffraction microscopy," Appl. Phys. Lett. **96**, 091102 (2010).
17. M. Guizar-Sicairos, S. Narayanan, A. Stein, M. Metzler, A. R. Sandy, J. R. Fienup, and K. Evans-Lutterodt, "Measurement of hard X-ray lens wavefront aberrations using phase retrieval," Appl. Phys. Lett. **98**, 111108 (2011).
18. S. Hönig, R. Hoppe, J. Patommel, A. Schropp, S. Stephan, S. Schöder, M. Burghammer, and C. G. Schroer, "Full optical characterization of coherent x-ray nanobeams by ptychographic imaging," Opt. Express **19**, 16324–16329 (2011).
19. G. Ingold, M. Boege, W. Bulgheroni, A. Keller, J. Krempaski, C. Schulze-Briese, L. Schulz, T. Schmidt, D. Zimoch, T. Hara, T. Tanaka, and H. Kitamura, "Performance of small-gap undulators at the SLS intermediate energy storage ring," AIP Conf. Proc. **879**, 388–391 (2007).
20. A. Menzel, C. M. Kewish, P. Kraft, B. Henrich, K. Jefimovs, J. Vila-Comamala, C. David, M. Dierolf, P. Thibault, F. Pfeiffer, and O. Bunk, "Scanning transmission X-ray microscopy with a fast framing pixel detector," Ultramicroscopy **110**, 1143–1147 (2010).
21. B. Henrich, A. Bergamaschi, C. Brönnimann, R. Dinapoli, E. F. Eikenberry, I. Johnson, M. Kobas, P. Kraft, A. Mozzanica, and B. Schmitt, "PILATUS: A single photon counting pixel detector for X-ray applications," Nucl. Instrum. Meth. A **607**, 247–249 (2009).
22. P. Kraft, A. Bergamaschi, C. Brönnimann, R. Dinapoli, E. F. Eikenberry, H. Graafsma, B. Henrich, I. Johnson, M. Kobas, A. Mozzanica, C. M. Schlepütz, and B. Schmitt, "Characterization and calibration of PILATUS detectors," IEEE Trans. Nucl. Sci. **56**, 758–764 (2009).
23. K. Jefimovs, J. Vila-Comamala, T. Pilvi, J. Raabe, M. Ritala, and C. David, "Zone-doubling technique to produce ultrahigh-resolution X-ray optics," Phys. Rev. Lett. **99**, 264801 (2007).
24. J. Vila-Comamala, S. Gorelick, V. A. Guzenko, E. Färm, M. Ritala, and C. David, "Dense high aspect ratio hydrogen silsesquioxane nanostructures by 100 kev electron beam lithography," Nanotechnology **21**, 285305 (2010).
25. F. van der Veen and F. Pfeiffer, "Coherent X-ray scattering," J. Phys.: Condens. Matter **16**, 5003–5030 (2004).
26. T. Aaltonen, M. Ritala, V. Sammelselg, and M. Leskelä, "Atomic layer deposition of iridium thin films," J. Electrochem. Soc. **151**, G489–G492 (2004).
27. O. Bunk, M. Dierolf, S. Kynde, I. Jonhson, O. Marti, and F. Pfeiffer, "Influence of the overlap parameter on the convergence of the ptychographical iterative engine," Ultramicroscopy **108**, 481–487 (2008).
28. M. Dierolf, P. Thibault, A. Menzel, C. M. Kewish, K. Jefimovs, I. Schlichting, K. von König, O. Bunk, and F. Pfeiffer, "Ptychographic coherent diffractive imaging of weakly scattering specimens," New J. Phys. **12**, 035017 (2010).
29. M. Guizar-Sicairos and J. R. Fienup, "Phase retrieval with transverse translation diversity: a nonlinear optimization approach," Opt. Express **16**, 7264–7278 (2008).
30. A. M. Maiden, M. J. Humphry, F. Zhang, and J. M. Rodenburg, "Superresolution imaging via ptychography," J. Opt. Soc. Am. A **28**, 604–612 (2011).
31. P. Thibault, V. Elser, C. Jacobsen, D. Shapiro, and D. Sayre, "Reconstruction of a yeast cell from X-ray diffrac-

#152217 - $15.00 USD Received 9 Aug 2011; revised 9 Sep 2011; accepted 12 Sep 2011; published 12 Oct 2011

tion data," Acta Cryst. A **62**, 248–261 (2006).
32. H. N. Chapman, A. Barty, S. Marchesini, A. Noy, S. P. Hau-Riege, C. Cui, M. R. Howells, R. Rosen, H. He, J. C. H. Spence, U. Weierstall, T. Beetz, C. Jacobsen, and D. Shapiro, "High-resolution ab initio three-dimensional X-ray diffraction microscopy," J. Opt. Soc. Am. A **23**, 1179–1200 (2006).
33. K. Giewekemeyer, P. Thibault, S. Kalbfleisch, A. Beerlink, C. M. Kewish, M. Dierolf, F. Pfeiffer, and T. Salditt, "Quantitative biological imaging by ptychographic X-ray diffraction microscopy," Proc. Natl. Acad. Sci. USA **107**, 529–534 (2010).
34. W. O. Saxton and W. Baumeister, "The correlation averaging of regularly arranged bacterial cell envelop protein," J. Microsc. **127**, 127–138 (1982).
35. M. van Heel and M. Schatz, "Fourier shell correlation threshold criteria," J. Struct. Biol **151**, 250–262 (2005).
36. M. Guizar-Sicairos, S. T. Thurman, and J. R. Fienup, "Efficient subpixel image registration algorithms," Opt. Lett. **33**, 156–158 (2008).
37. M. Guizar-Sicairos, A. Diaz, M. Holler, M. S. Lucas, A. Menzel, R. A. Wepf, and O. Bunk, "Phase tomography from X-ray coherent diffractive imaging projections," Opt. Express (to be published).
38. J. W. Goodman, *Introduction to Fourier Optics*, 2nd ed., (The McGraw-Hill Companies, Inc., New York, 1996) Chap. 3, Foundations of Scalar Diffraction Theory, pp. 55–62.

1. Introduction

Advances in the manufacture of high-resolution X-ray optics [1–3] capable of focusing X-ray beams into focal spots of a few tens of nanometers in size requires the development of new characterization methods. Conventional techniques such as the use of knife-edge scans or well-characterized test objects cannot achieve a full evaluation of the performance of the focusing device. Furthermore, such techniques can only provide limited feedback for improvements in the fabrication technology and alignment routines of nanofocusing X-ray optics. Coherent diffractive imaging (CDI) and phase retrieval techniques [4–6] offer the unique capability of retrieving the complex-valued wavefield distribution of electron, visible light and X-ray wavefronts from one or more far-field intensity measurements. Although CDI methods were initially intended to overcome the spatial resolution limitations of lens-based imaging of the sample under study [7, 8], they have also been proven as a very effective approach to gain insight of the incident X-ray beam illuminating the object [2, 9, 10]. In particular, ptychographic coherent diffractive imaging (PCDI) techniques [11–13] have been demonstrated as a compelling method to assess the quality of the nanofocused X-ray beams and evaluate the performance of high-resolution X-ray optics such as mirrors [14, 15] and refractive lenses [16–18].

In this work we used PCDI to investigate the focusing capabilities of a high-resolution diffractive X-ray lens, i.e., a Fresnel zone plate (FZP), capable of focusing multi-keV X-rays into a round focal spot 23 nm wide [3]. Ptychographic scans on a nanopatterned object were employed to reconstruct the X-ray complex-valued wavefield of the out-of-focus illumination provided by the high-resolution FZP. By numerically propagating the reconstructed wavefield along the optical axis to the focal plane, we have obtained a full characterization of the focusing performance of the FZP. Furthermore, by propagating the wavefield to the exit pupil of the diffractive lens, we can evaluate the wavefront aberrations both related to its manufacture and the upstream beamline optics. These results demonstrate that PCDI is an excellent method to characterize high-resolution diffractive X-ray optics and provides valuable feedback for improvements of manufacturing and alignment procedures.

2. Experimental Methods

The experiments were carried out at the coherent small angle X-ray scattering (cSAXS) beamline of the Swiss Light Source, Paul Scherrer Institut. Figure 1(a) shows the scheme of the experimental setup employed to acquire the ptychographic data. The X-ray beam was extracted from an U19 undulator insertion device [19] with an estimated photon source size of 200×20 μm^2 horizontal$\times$vertical (H$\times$V) full width at half maximum (FWHM). A

#152217 - $15.00 USD Received 9 Aug 2011; revised 9 Sep 2011; accepted 12 Sep 2011; published 12 Oct 2011

double-crystal Si(111) monochromator selected a photon energy of 6.20 keV (wavelength, $\lambda = 0.200$ nm), and the X-ray beam was delivered into the experimental hutch after being reflected by a grazing-incidence mirror, to reject higher-order harmonics, and passing through several sets of beam-conditioning slits. The setup in the experimental hutch was identical to a scanning transmission X-ray microscope [20]: it comprised a central stop, a high-resolution FZP, a 10 μm diameter pinhole serving as order selecting aperture (OSA), and the object, which was mounted on a high-precision piezoelectric positioning stage for high-resolution scanning. A pixelated PILATUS 2M detector was located at a distance $d_{sam-det} = 2253$ mm downstream of the object position, behind a He-filled flight tube to prevent excessive absorption and scattering by air. The PILATUS 2M detector sampled the far-field intensity with 1475×1679 pixels of size 172×172 μm^2, having 20-bit dynamic range, no readout noise, and a point spread function of one single pixel [21, 22]. The detector, operated in single-photon counting mode, was used to record the full divergent radiation cone created by the FZP and scattered photons emanating from the object.

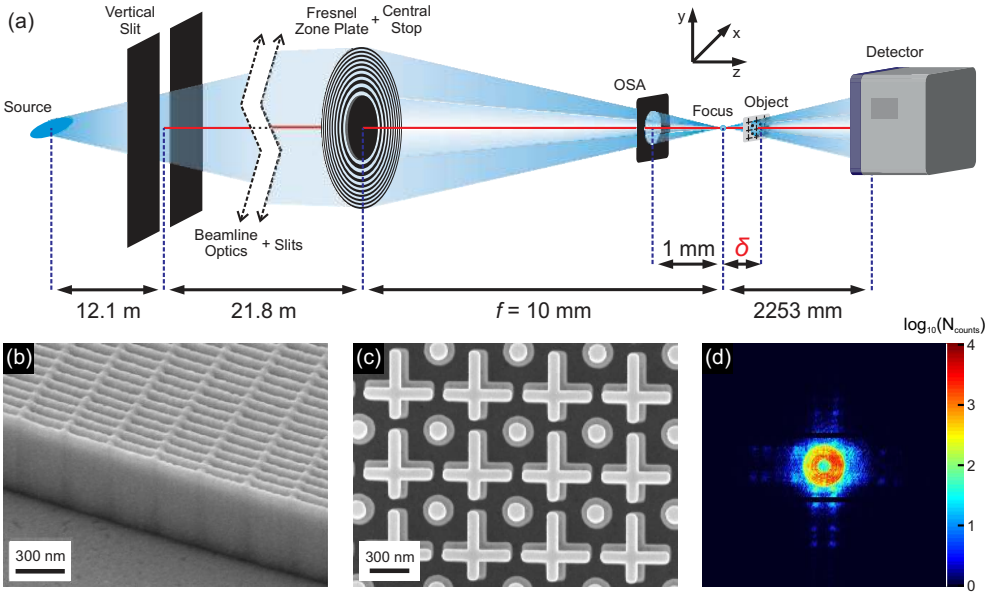

Fig. 1. (Color online) (a) Experimental setup employed for Fresnel zone plate characterization by ptychographic coherent diffractive imaging, sketch not drawn to scale. (b) Scanning electron micrograph showing the outermost region of the Fresnel zone plate made of zone-doubled iridium structures of 20 nm width and 550 nm height. (c) Scanning electron micrograph showing the nanofabricated pattern made of silicon oxide and iridium that was used as object. (d) Example of a diffraction pattern frame acquired by the PILATUS 2M detector at one position of the ptychographic scan.

The high-resolution FZP used to focus the incoming X-ray beam had a diameter of $D = 100$ μm and an outermost zone width of 20 nm. It was made of iridium and its zone height was approximately measured to be 550 nm. This diffractive optical element was manufactured by means of a zone-doubling technique [23], and further details of its fabrication and characterization can be found in Refs. [24] and [3], respectively. Figure 1(b) shows a scanning electron microscopy (SEM) image of the outermost region of the zone-doubled iridium structures, consisting of 20 nm lines and spaces. The zone-doubled FZP was designed to have a focal length of $f = 10.0$ mm at a photon energy of 6.2 keV and its focusing diffraction effi-

#152217 - $15.00 USD Received 9 Aug 2011; revised 9 Sep 2011; accepted 12 Sep 2011; published 12 Oct 2011

ciency was experimentally measured to be 6.3% for this photon energy in previous experiments. An 18 μm-thick central stop roughly 35 μm in diameter was mounted on an additional stage about 4 mm upstream of the FZP position. A relevant detail in the setup is that the zone-doubled FZP was located at about 34 m from the source, at which point the incident X-ray beam was expected [25] to have a transverse coherence area of 25×250 μm^2 (H×V of FWHM). The horizontal dimension was thus too small to provide coherent illumination of the FZP aperture. To overcome this limitation, at expense of a reduced photon flux, a vertical slit located at 12.1 m downstream of the undulator source was used to create a secondary source and increase the transverse coherence in the horizontal direction, as shown in Fig. 1(a). The nominal slit width was set to 25 μm while acquiring the ptychographic data. Thus, unlike in previous experiments [12], the zone-doubled FZP was fully rather than partially illuminated by the incident coherent X-ray beam, and it was expected to create a diffraction-limited focusing round spot of 20.6 nm in size (FWHM). Notice that due to the use of the central stop and the OSA only the 1^{st} diffraction order of the FZP contributes to the illumination of the object. Thus, we are only investigating the focal spot and wavefield of the 1^{st} diffraction order of the FZP.

The strongly scattering object was a nanofabricated pattern made of silicon oxide and iridium by combining electron beam lithography and atomic layer deposition [26]. Initially, the silicon oxide structures were fabricated by electron beam lithography with a smallest feature size of about 50 nm. After that, the pattern was conformally coated with a 17 nm-thick layer of iridium to enhance its X-ray scattering cross-section. As a result, the silicon oxide structures were buried beneath a uniform iridium film covering both ridges and sidewalls of the original pattern. Figure 1(c) shows an SEM image of the object, in which only the uniform superficial iridium layer is revealed.

Prior to the ptychographic scans we used scanning transmission X-ray microscopy to determine the focal plane position for the 1^{st} diffraction order of the FZP. The position of the object along the optical axis could thus be precisely chosen. For the ptychographic scans the object was moved downstream from the focal plane by a distance $\delta = 75$ μm. Scanning the object with an out-of-focus illumination function was convenient to increase the size of the illuminated area of the object to roughly $S = \delta\frac{D}{f} = 750$ nm and allow larger scanning steps while preserving sufficient overlap of neighboring illuminated positions [27] and adequate sampling of the resulting speckle pattern by the PILATUS 2M detector. The diffraction patterns were collected by scanning a 2×2 μm^2 area of the object in concentric circles [28], whose radii varied from 0.2 to 1 μm in steps of 0.2 μm. The scan started at the center position, and each circle contained five more positions than the previous one. In this manner, 83 diffraction patterns, like the one shown in Fig. 1(d), were collected with 0.5 s acquisition time each. A second scan was recorded immediately after translating the detector to a second position in order to acquire the information missing in the diffraction patterns due to the gaps between contiguous modules of the PILATUS 2M detector. In total, 166 diffraction patterns were collected in slightly less than 2 min for each ptychographic scan.

From the original full frames acquired by the PILATUS 2M detector, we selected a square window of 800×800 pixels centered at the radiation cone of the FZP as input data for the reconstruction algorithm. The pixel size in the reconstructed image and probe, i.e., the complex-valued wavefield of the illumination function at the object position, was $s_{pixel} = \frac{\lambda \cdot d_{sam-det}}{800 \cdot a_{pixel}} = 3.27$ nm where $a_{pixel} = 172$ μm is the detector pixel size. The ptychographic reconstructions of the object and probe were simultaneously obtained by the difference-map phase retrieval algorithm [12, 13] after 300 iterations and an average computing time of 2 hours. The reconstructed object image was taken as the average of 20 reconstructions picked between the 200th and the 300th iteration [28]. This averaging reduced the contribution of fluctuating features that were not consistent as the iterations progressed. The result from the difference-map algorithm

#152217 - $15.00 USD Received 9 Aug 2011; revised 9 Sep 2011; accepted 12 Sep 2011; published 12 Oct 2011

was then refined through a maximum likelihood non-linear optimization [29]. This combination exploits the ability of the difference-map algorithm to quickly explore the solution space, effectively converging to the neighborhood of the solution but usually oscillating around it. The optimization is then used as a refinement step to retrieve an optimal solution in this neighborhood by explicitly accounting for the Poisson statistics of the detection noise in the measurement. Additionally, for these reconstructions we used an optimization error metric that is insensitive to fluctuations of the total beam intensity, such that these possible fluctuations bear no effect on reconstruction progress. This combination of the difference-map followed by optimization refinement yielded improved object image quality, reduced noise and increased reproducibility in the reconstructed illumination function. Further details of this non-linear optimization refinement will be published elsewhere.

The two ptychographic scans, acquired at different lateral detector positions, were simultaneously used by the phase retrieval algorithms. Using the known detector translation we matched the center of the diffraction patterns for both scans, and defined accordingly translated binary masks that denoted where data from the module gaps was missing, i.e., the mask was unity where data was measured and zero otherwise. The Fourier domain projection used by the difference-map took into account these masks by imposing the measured intensity where the corresponding mask was unity and leaving the amplitude unchanged at the gaps, an approach used in Ref. [12] to deal with detector dead pixels. For the optimization refinement we used a weighting function that excluded the pixels in the gaps from the computation of the error metric, an approach that was described in Ref. [29] and experimentally proven in Ref. [14]. Because the detector was moved between the two scans most of the data points lost due to the detector gaps in the first position are measured in the second detector position. That is, most points in Fourier domain were actually constrained by at least one measurement, thereby having only small (7x17 pixels) regions of missing data at relatively high diffraction angles. Given the ability of PCDI to extrapolate measurements to achieve super-resolution [30] it is expected that these small regions of missing data bear a small effect on the reconstructions. This approach also placed the adequate higher emphasis for the points in the diffraction patterns that were measured twice and avoids spurious edges that may appear for more conventional stitching methods and could have a detrimental effect on image quality.

3. Results and Discussion

3.1. Object Image Reconstruction

Although the main interest of this work is the characterization of the illumination function delivered by the high-resolution FZP, the retrieved image of the nanopatterned object can be used to assess the quality and reproducibility of the reconstruction method. Figure 2(a) shows the reconstructed phase image of the nanopatterned object. This image was obtained from the average of two consecutive separate ptychographic scans that were acquired under the same conditions but independently reconstructed. As discussed below in detail, these two repeated images of the same area of the object were retrieved to quantitatively assess image quality while accounting for different noise realization in the measurements and experimental errors such as vibrations or fluctuations in the illumination. The reconstructed phase image in Fig. 2(a) demonstrates very good agreement with the SEM picture shown in Fig.1(c). The ptychographic reconstruction can clearly resolve the smallest separation between sharp features, which is about 40 nm. In addition, the high contrast dark lines at the edges of the structure correspond to the 17 nm wide iridium layer conformally covering the buried silicon oxide structure that is not visible in the SEM picture. The object image power spectrum, i.e., the squared-modulus of its Fourier transform depicted in Fig. 2(b), shows that significant signal is obtained above the noise level for more than half of the computational window, corresponding to a half-cycle resolution of

#152217 - $15.00 USD Received 9 Aug 2011; revised 9 Sep 2011; accepted 12 Sep 2011; published 12 Oct 2011

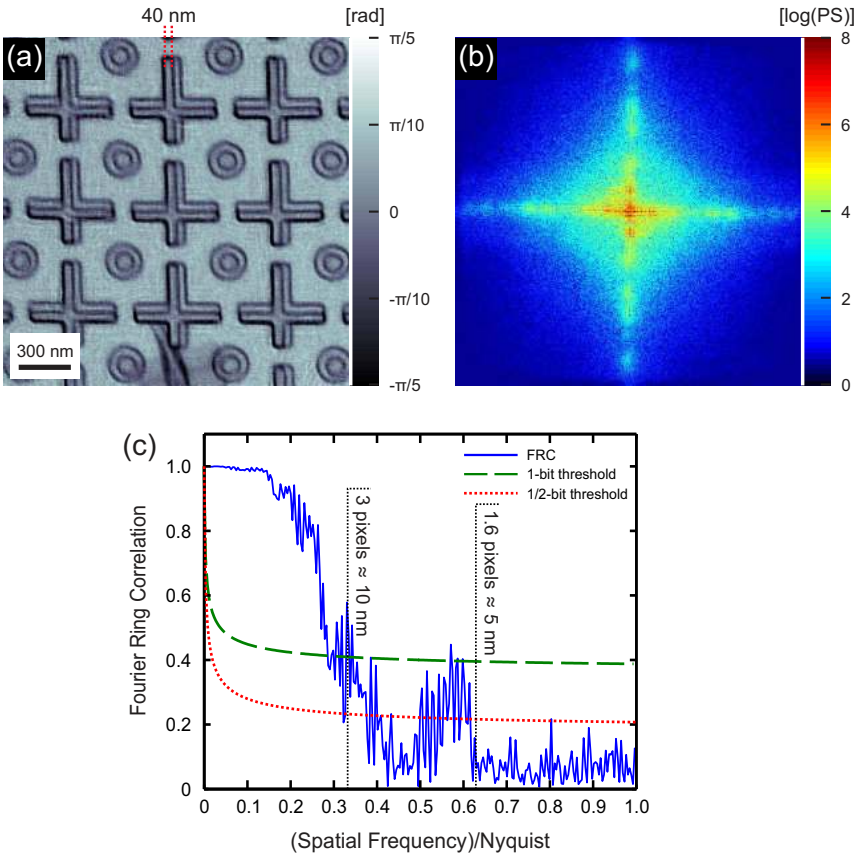

Fig. 2. (Color online) (a) Ptychographic reconstructed phase image of the object consisiting of nanofabricated structures made of silicon oxide and iridium. (b) Power spectrum of the phase object image. (c) Fourier ring correlation (FRC) plot demonstrating a spatial resolution of 8 nm in the phase image of the object reconstruction.

2 pixels, or 6.6 nm, for both horizontal and vertical directions. However, a more accurate estimation of spatial resolution directly from the reconstructed image is difficult in this case since the actual sharpness of the features in the object is coarser than the spatial resolution.

In general, assessing the quality and the spatial resolution of reconstructed object images obtained by CDI algorithms is an important task. For CDI techniques involving a single diffraction pattern a commonly used tool is the phase retrieval transfer function (PRTF) [31, 32], which gives a measure of the consistency of the retrieved phases in the Fourier domain for either different number of iterations or different random starting guesses of the object. In PCDI, the diffraction patterns are contributed by the two unknown functions that are being retrieved, namely the object and the probe, and it is then difficult to distinguish if the PRTF is associated to the object or the probe. In addition, it has been pointed out that for PCDI the PRTF can be significantly misleading for the reconstruction of weak scattering objects [28, 33].

Here, we have estimated the spatial resolution in the reconstructed object image using Fourier ring correlation (FRC, also referred as Fourier shell correlation for its extension to three-dimensional imaging) [34, 35]. The FRC approach is a well-established technique for determining the spatial resolution of two- and three-dimensional images in transmission electron

#152217 - $15.00 USD Received 9 Aug 2011; revised 9 Sep 2011; accepted 12 Sep 2011; published 12 Oct 2011

microscopy. It provides a curve of the normalized cross-correlation coefficient between two independently acquired images at a given ring in the reciprocal space, hence giving a measure of the consistency of the image signal as a function of the spatial frequency, or resolution. As the signal-to-noise ratio (SNR) for a particular spatial resolution is reduced, so is the FRC curve. To compute the FRC, two independent datasets were measured and reconstructed. Because the reconstructed object images can have a translation error between them, they were aligned with subpixel precision using an efficient image registration method based on cross-correlation [36]. Additionally, before the computation of the FRC a global and linear phase terms should be matched between the images, as these terms are inherent ambiguities for PCDI when both object image and illumination function are retrieved [37]. Finally, the edges of the object images were multiplied by a soft-edged mask in order to avoid the introduction of artificially sharp similarities at the edge of the computational window [35]. The FRC computed from these images, as function of spatial frequency, is shown with a solid line in Fig. 2(c). To give a quantitative estimate of the image resolution from the FRC a threshold curve can be used. The threshold curve chosen here is an analytical expression independent of the image data for the expected FRC for images with a SNR that is constant in the Fourier domain [35]. The threshold curve shown in Fig. 2(a) with a dotted line corresponds to the $1/2$-bit criterion, that is, a flat SNR of 0.41 in the Fourier domain. This criterion was introduced in Ref. [3] as a metric that produces similar results as other tools currently used to estimate the resolution for X-ray crystallography. Figure 2(c) shows that the FSC cuts the threshold curve at a spatial frequency corresponding to a spatial resolution of about 8 nm, which indicates that at such resolution the SNR in the average image, shown in Fig. 2(a), drops below the threshold value. It is also remarkable that the FRC remains comparable to the $1/2$-bit threshold curve at spatial frequencies down to 5 nm. A more conservative estimate of 12 nm resolution is given by the 1-bit threshold curve in Fig. 2(c), which corresponds to a SNR of unity. From these FRC results and the image power spectrum we estimate a spatial resolution of 8 nm in the reconstructed phase image of the object.

3.2. Focal Spot Wavefield and Wavefront Reconstruction

Ptychographic phase retrieval algorithms reconstruct both the object image, i.e., the complex-valued object transmission function, and the probe, the latter being the illuminating complex-valued wavefield at the object position. We can characterize the focal spot wavefield and lens wavefront aberrations corresponding to the 1^{st} diffraction order of the high-resolution FZP by appropriately back-propagating the reconstructed probe along the optical axis.

As described in Sec. 2, the object was nominally located at a distance $\delta = 75$ μm from the focal plane. At this position, the X-ray beam was expected to be defocused with an expected size of $S = 750$ nm. Figure 3(a) shows the intensity distribution of the reconstructed wavefield at this object position. Although the probe lacks uniformity and well-defined boundaries, we can estimate the defocused X-ray beam size to be approximately 650 nm, thus slightly smaller than expected. From the complex-valued wavefield at this position, the X-ray beam wavefield at the vicinity of the focal plane can be numerically calculated by employing the angular spectrum approach [38], which involves computing the Fourier spectrum of the wavefield by means of a discrete Fourier transform (DFT), applying a multiplicative propagation transfer function and returning to the real space using an inverse DFT. Figure 3(b) shows the intensity of the propagated wavefield of the planes XZ and YZ through the focus of the high-resolution FZP (the Z direction is taken along the optical axis of the experimental setup, as depicted in Fig. 1). In the plots, the intensity is shown on a logarithmic scale, to reveal more detail, and dashed lines mark the locations of the object and approximate focal plane (as labeled). The location of the peak intensity in the propagated wavefield indicates that the actual distance of the focus to the object was about 68 μm. This value, slightly shorter than the nominal $\delta = 75$ μm, is consistent

#152217 - $15.00 USD Received 9 Aug 2011; revised 9 Sep 2011; accepted 12 Sep 2011; published 12 Oct 2011

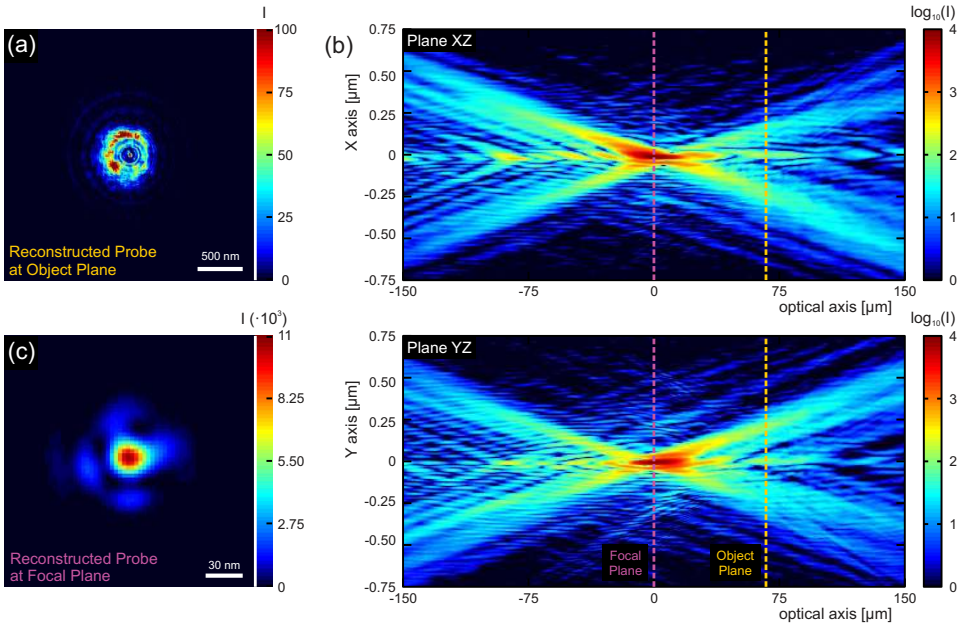

Fig. 3. (Color online) (a) Intensity of the reconstructed illumination function at the object plane. (b) Propagation along the optical axis of the X-ray beam at the vicinity of the focal plane of the high-resolution Fresnel zone plate. (c) Wavefield intensity distribution at the focal plane. The size of the focal spot is estimated to be 22.5×23.8 nm^2 (H$\times$V of FWHM).

with the observed smaller size of the probe in the object plane. The discrepancy between the nominal and the retrieved values of δ can be explained by inaccuracies during the determination of the focal position by scanning transmission X-ray microscopy, and it is within the range of the expected depth of focus (DOF) of 8 μm. Lens aberrations, in particular astigmatism, can hinder the determination of the focal plane by scanning transmission X-ray microscopy. The wavefield intensity at the focal plane is shown in Fig. 3(c). The size of the focal spot is estimated to be 22.5×23.8 nm^2 (H$\times$V of FWHM). These retrieved values are close to the expected size of 20.6 nm (FWHM) for FZP with an outermost zone width, Δr, of 20 nm.

The imperfections on the focused wavefield, observed in Figs. 3(b) and 3(c), arise from aberrations of the wavefront exiting the high-resolution FZP. To investigate these aberrations, we back-propagate the reconstructed wavefield upstream to the exit pupil of the lens. This is most efficiently achieved, in terms of sampling requirements, by computing the Fresnel diffraction integral [9, 38] using a single DFT. Propagating the reconstructed probe by 10 mm upstream in this manner we obtain the wavefield at the exit pupil with a sampling of about 1.0 μm. The amplitude of the wavefield exiting the FZP is shown in Fig. 4(a). From the phase of this complex-valued wavefield, one can subtract the constant, linear and quadratic phase terms. The resulting phase profile, shown in Fig. 4(b), reveals the wavefront aberrations, i.e., the deviations between the exit wave and a perfectly spherical wave which would be expected for an ideal lens. By inspection of the wavefront aberrations one can distinguish high- and low-frequency variations. The low-frequency components are most likely introduced by the upstream optical elements of the beamline. The beam-conditioning slits or imperfections of the monochromator and mirror used for higher-order harmonic rejection are believed to create the non-uniform intensity and the vertical and horizontal stripes observed on the amplitude of the lens wavefield

#152217 - $15.00 USD Received 9 Aug 2011; revised 9 Sep 2011; accepted 12 Sep 2011; published 12 Oct 2011

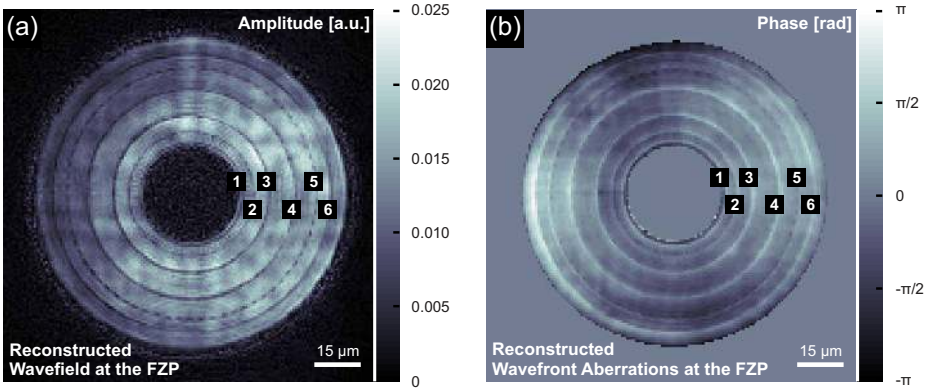

Fig. 4. (a) Amplitude and (b) wavefront aberrations at the exit pupil of the high-resolution Fresnel zone plate. The root mean square in the wavefront aberrations are found to be 0.7213 rad (0.1148 waves). The numbering indicates the radial positions where buttressing periodicity is changed and relates to Fig. 5.

in Fig. 4(a). The low-frequency components in the lens wavefront aberrations in Fig. 4(b) are clearly dominated by astigmatism, which is characterized by a curvature of opposite signs in orthogonal directions, i.e., a saddle shaped function. This astigmatism is produced by a slight vertical focusing of the higher-order harmonic rejection mirror, which then delivers a slightly aberrated beam to the FZP. On the propagated X-ray beam, in Fig. 3(b), this astigmatism results in a slight difference in distance from the lens to the best focal planes in the X and Y directions. The latter difference made the determination of best focus difficult with the STXM, whereas with the reconstructed beam the determination of the best focus becomes easier by using the circle of least confusion, i.e., the plane where the area inside the FWHM intensity contour is minimized.

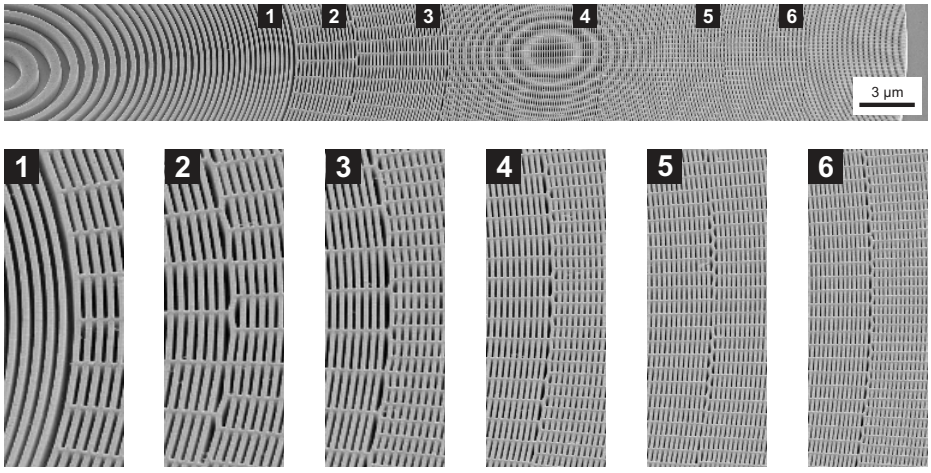

Fig. 5. Scanning electron micrographs of the high-resolution zone-doubled Fresnel zone plate. Insets show magnified images at radial positions where the buttressing periodicity is changed.

#152217 - $15.00 USD Received 9 Aug 2011; revised 9 Sep 2011; accepted 12 Sep 2011; published 12 Oct 2011

On the other hand, the high-frequency aberrations are more likely to originate from the FZP structure. In the upper-left quadrant of both the amplitude and the phase aberration plots in Fig. 4 one observes the shadows of a square grid with an approximate period of about 5 μm. This periodicity matches the writing field of the electron beam lithography tool that was used to fabricate the FZP pattern. Such imperfections, usually not visible under SEM inspection, are due to small changes of the exposure parameters between contiguous writing fields. These errors are known in the electron beam lithography community as sub-field stitching error. A second pattern that is obvious in the reconstructed wavefront aberrations are the six concentric rings occurring at increasing radii. They can be easily related to deviations from the ideal FZP structure, i.e., any misplaced zones that will result on perturbations of the phase of the wavefield exiting the FZP. However and due to the large pixel size, only the average effect of these phase perturbations can be observed on the reconstructed wavefield. Figure 5 shows SEM pictures of the FZP, highlighting the buttresses which are necessary to create mechanically stable, high aspect ratio resist structures during the electron beam lithography step [3]. It was experimentally determined that the most stable structures to connect neighboring zones were buttresses radially aligned with the FZP pattern. However, to maintain sufficiently short azimuthal space between the buttresses, their periodicity had to be adjusted as a function of the radial position. The FZPs were fabricated containing six discrete buttressing periodicity changes as shown in Fig. 5. The reconstructed wavefront reveals that each of the buttressing periodicity changes creates a unique imperfection in the wavefront exiting the FZP. Closer to the edge of the FZP, the similarity between the azimuthal separation of the buttresses in neighboring regions creates a beating between the spatial frequencies, resulting in a discontinuous line in the wavefront aberrations at the position of the rings. The latter effect is most noticeable in ring 5, as indicated in Figs. 4 and 5. While the SEM inspection only demonstrates the deformation of about 4 to 6 iridium zones at each buttressing periodicity change, the current analysis might suggest that a larger number of zones are misplaced. This information will be used in designing an improved buttressing pattern to reduce the aberrations in future fabrication of FZPs.

The wavefront aberrations exiting the FZP were found to have a root mean square (RMS) value of 0.7213 rad or 0.1148 waves. For comparison, the Maréchal criterion establishes that the phase accuracy required for diffraction-limited performance is $1/14 = 0.072$ waves RMS. This indicates that the reconstructed X-ray beam was not diffraction-limited and it is consistent with the deviations in size and shape of the reconstructed focal spot with respect to an ideal Airy function. However, the wavefront analysis we have performed already points to a few issues in the lens manufacture and in the incident X-ray beam conditioning that could be addressed to achieve diffraction-limited focusing. Upon comparison from two ptychographic reconstructions of independently acquired datasets we found the wavefront aberration measurement to be repeatable to within an RMS error of 0.04 rad (i.e., 0.006 waves), thus giving assurance of the effectiveness and precision of the method. Such high degree of repeatibility on the wavefront aberration measurement was only achieved after applying the non-linear optimization refinement. Upon comparison from the two ptychographic reconstructions using only the difference-map phase retrieval algorithm of the same datasets, the wavefront aberrations measurements were only repeatable to within an RMS error of 0.145 rad (i.e., 0.023 waves), that is the non-linear optimization refinement accounted for more than a three-fold improvement in the consistency of the two wavefront aberration reconstructions of independently acquired data.

4. Summary and Conclusions

In this work we have demonstrated the feasibility of characterizing high-resolution diffractive X-ray optics by PCDI. We have used this method to successfully reconstruct the 23 nm wide focal spot delivered by a zone-doubled FZP. Simultaneously, we have investigated the wavefront

#152217 - $15.00 USD Received 9 Aug 2011; revised 9 Sep 2011; accepted 12 Sep 2011; published 12 Oct 2011

aberrations at the exit pupil of the lens, which are related both to manufacturing aspects of the FZP and imperfections on the incident X-ray wavefront introduced by the upstream beamline optics. Both sources of aberration affect negatively the quality of the focal spot. These results further consolidate PCDI as a robust and accurate method to measure aberrations of X-ray optics [14, 17] and demonstrate that it is an excellent tool to assess the performance of FZP, while providing valuable feedback beyond conventional characterization techniques. Furthermore, since the ptychographic scans can be realized in less than 2 min and the ptychographic reconstructions times can be shorten from 2 hours to about 20 min by taking a smaller window of PILATUS frames (400×400 pixels), the technique is well-suited for *in-situ* and on-line alignment and optimization of the experimental setups.

Acknowledgments

We acknowledge the contributions of P. Thibault, M. Dierolf, and F. Pfeiffer (now at the Technical University Munich) to the difference-map code for ptychographic reconstructions. We would like to thank A. Weber, B. Haas, V. A. Guzenko (Paul Scherrer Institut) for assistance during the substrate preparation and X. Donath (Paul Scherrer Institut) for technical assistance at the beamline. Alexandre Mantion thanks the Adolf-Martens-Fonds e.V., the BAM Federal Institute for Materials Research and Testings for financial support and the DFG grant for Initiation and Intensification of Bilateral Cooperation under project number MA-5217/3-1. The research leading to these results has received funding from the European Community's Seventh Framework Programme (FP7/2007-2013) under grant agreement No. 226716.

#152217 - $15.00 USD Received 9 Aug 2011; revised 9 Sep 2011; accepted 12 Sep 2011; published 12 Oct 2011